


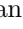














# Energies and lifetimes of the 9p and 10p excited states in atomic francium

P. Lassègues <sup>1,\*</sup> A. Ajayakumar,<sup>2</sup> M. Athanasakis-Kaklamanakis <sup>3</sup> O. Ahmad,<sup>1</sup> M. Au <sup>2,4</sup> J. Berbalk,<sup>1,2</sup> D. Bettaney,<sup>5</sup> B. van den Borne <sup>1</sup> A. Chakraborty <sup>6</sup> T.E. Cocolios <sup>1</sup> M. Duggan,<sup>5</sup> C. Fajardo <sup>1,7</sup> K.T. Flanagan <sup>5</sup> R.F. Garcia Ruiz,<sup>8,9</sup> R. de Groote <sup>1</sup> D. Gonzalez-Acevedo,<sup>8</sup> A. Kastberg,<sup>10</sup> A. Koszorús,<sup>1</sup> L. Lalanne,<sup>11</sup> K.M. Lynch <sup>5</sup> D.T. McLeroy,<sup>5</sup> A. McGlone <sup>5</sup> G. Neyens <sup>1</sup> L. Nies <sup>7</sup> L. Quanjel,<sup>1,12</sup> A. Raggio <sup>1</sup> J. Reilly,<sup>5</sup> B.K. Sahoo <sup>6</sup> J. Snikeris,<sup>13,14</sup> J. Warbinek,<sup>7</sup> S.G. Wilkins,<sup>8</sup> and X.F. Yang <sup>15</sup>

<sup>1</sup>*KU Leuven, Instituut voor Kern-en Stralingsfysica, 3001, Leuven, Belgium*

<sup>2</sup>*Systems Department, CERN, CH-1211 Geneva 23, Switzerland*

<sup>3</sup>*JILA and University of Colorado, Boulder, Colorado 80309, USA*

<sup>4</sup>*Department of Chemistry, Johannes Gutenberg-Universität Mainz, 55099 Mainz, Germany*

<sup>5</sup>*Department of Physics and Astronomy, The University of Manchester, Manchester M13 9PL, United Kingdom*

<sup>6</sup>*Physical Research Laboratory, Ahmedabad-380009, India*

<sup>7</sup>*Experimental Physics Department, CERN, CH-1211 Geneva 23, Switzerland*

<sup>8</sup>*Department of Physics, Massachusetts Institute of Technology, Cambridge, Massachusetts 02139, USA*

<sup>9</sup>*Laboratory for Nuclear Science, Massachusetts Institute of Technology, Cambridge, Massachusetts 02139, USA*

<sup>10</sup>*Institut de Physique de Nice, Université Côte d'Azur, 06108 Nice, France*

<sup>11</sup>*Université Paris-Saclay, CNRS/IN2P3, IJCLab, Orsay, F-91405, France*

<sup>12</sup>*Belgian Nuclear Research Centre, SCK CEN, 2400 Mol, Belgium*

<sup>13</sup>*Department of Physics, University of Gothenburg, 412 96 Gothenburg, Sweden*

<sup>14</sup>*Institute of Atomic Physics and Spectroscopy, University of Latvia, 1004 Riga, Latvia*

<sup>15</sup>*School of Physics and State Key Laboratory of Nuclear Physics and Technology, Peking University, Beijing, China*

(Dated: May 13, 2026)

We present the first measurement of  $9p^2P_{1/2,3/2}$  and  $10p^2P_{1/2,3/2}$  excited levels absolute wavenumbers and radiative lifetime in francium. We used the Collinear Resonance Ionization Spectroscopy (CRIS) technique, applied on a beam of  $^{221}\text{Fr}$  atoms. Prior to this work, no experimental data existed for francium p-states with  $n > 8$ . The results provide a precision experimental test of relativistic coupled-cluster theory for the heaviest alkali, showing good agreement for lifetimes and relative excitation energies, despite a residual global offset in absolute energies.

The search for physics beyond the standard model is pursued at a wide range of energy scales, from the highest experimentally obtainable [1], to ultra-high precision experiments at very low energies using molecular and atomic systems [2]. In the latter case, sought-after observables, such as the electron electric-dipole moment [3], parity non-conservation and the nuclear anapole moment [4, 5] tend to scale strongly with the atomic number  $Z$ . Francium, with  $Z = 87$ , is the heaviest alkali and therefore an attractive candidate for precision measurements of these symmetry-violating observables. A challenge, however, is that a substantial part of the energy spectrum of francium is unexplored, experimentally and theoretically, making it difficult to benchmark theoretical models, reliably interpret precision measurements, and extract fundamental parameters from experimental data.

Francium has recently attracted interest for studies of both nuclear spin-independent and spin-dependent parity violation to probe new physics and nuclear anapole moment [6–8]. Accurate knowledge of the E1 matrix elements is crucial for estimating atomic parity-violating amplitudes. The accuracy of theoretical calculations of these matrix elements can be tested by comparing to experimental data on lifetimes of atomic states [9].

Previous theoretical studies of francium have shown that excitation energies and transition properties are strongly affected by relativistic and electron-correlation

effects, with significant method-dependent corrections, particularly for highly excited states [10]. In the absence of accurate experimental benchmarks, theoretical approaches such as relativistic many-body perturbation theory and relativistic coupled-cluster theory cannot be rigorously tested, limiting the reliable extraction of observables relevant to precision tests of fundamental symmetries [10, 11]. While correlation trends have been studied for low-angular-momentum states, such as s-states [12, 13], they have not been explicitly demonstrated for higher-angular-momentum excited states in francium, such as p and d states.

For 9p and 10p, the wavenumber values published in the NIST Atomic Spectra Database [14], are semi-empirical, based on Biemont *et al.* [15] and are computed using a Rayleigh-Ritz formula. Isotope shifts are not taken into account in that work. *Ab initio* calculations of the 9p and 10p energies were reported in [16], and radiative lifetimes were calculated with a Coulomb approximation in [17].

In this work, we present the first experimental data on the 9p and 10p absolute wavenumbers, fine-structure splittings and radiative lifetimes, obtained with resonance ionization spectroscopy, for the isotope  $^{221}\text{Fr}$ . We also present new relativistic coupled-cluster *ab initio* calculations, significantly improved over previous theoretical efforts, performed for all experimental data

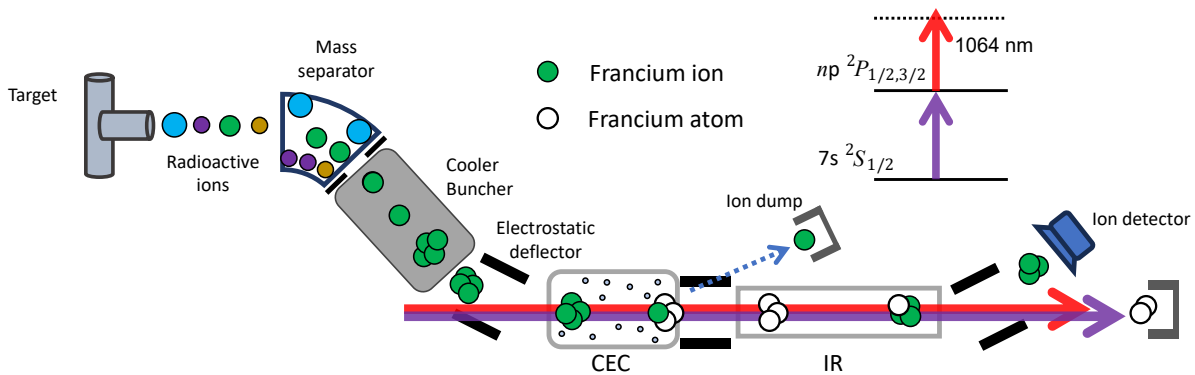


FIG. 1: Overview of the CRIS beam line, detailing the sequence of ion production, mass separation, bunching within a Paul trap (cooler buncher), neutralization via the charge-exchange cell (CEC), and resonant laser ionization in the interaction region (IR). Top-right: Example of a laser excitation sequence employed for francium in this study (shown here for excitation from ground state to a generic  $np\ 2P$  level)

presented in this work. The experimental procedure was benchmarked against previous measurements of the  $8p\ 2P_{3/2}$  state. This combined experimental and theoretical work enables us to verify the accuracy of calculations of E1 matrix elements, providing essential experimental input for atomic parity-violating amplitude measurements.

The experimental data were obtained at the Collinear Resonance ionization Spectroscopy (CRIS) experiment using a beam of  $^{221}\text{Fr}^+$  produced at the ISOLDE radioactive ion-beam facility at CERN. The radioactive isotopes were produced upon the impact of protons from the CERN Proton Synchrotron Booster onto an Uranium carbide target [18, 19]. After irradiation,  $^{221}\text{Fr}^+$  continued to be formed in the target, as part of the decay chain of the long-lived  $^{225}\text{Ac}$  and  $^{229}\text{Th}$ . By heating the target, francium atoms were released, and diffused into a hot-cavity surface ionization ion source, where they were ionised with near unity efficiency. The ions were accelerated to 30 keV, separated by their mass-to-charge ratio in the high-resolution separator magnets HRS [20], cooled and bunched in a gas-filled radio-frequency quadrupole linear Paul trap (ISCOOL) [21] and delivered to the experimental setup (Fig. 1) [22, 23]. Entering the CRIS experiment, they were neutralized in a charge-exchange cell (CEC) filled with sodium vapor. Non-neutralized ions were deflected to a beam dump. Neutralized francium atoms entered the interaction region where they were resonantly ionised via a two-step pulsed laser scheme (Fig. 1, top right). Ions were deflected onto a single ion counting detector, while the residual neutral beam was discarded. The ion beam was released from the cooler buncher with a repetition rate of 100 Hz, in bunches of  $5\ \mu\text{s}$  temporal width, which corresponds to a 0.8 m longitudinal spatial width. The ions were accelerated out of the cooler-buncher with a voltage of 29947.5(6)V. Light for the 422-nm  $7s\ 2S_{1/2} \rightarrow 8p\ 2P_{3/2}$  transition was produced

by external-cavity second-harmonic generation (SHG) from a pulsed Titanium:Sapphire (Ti:Sa) laser, which was pumped by a pulsed 532-nm laser at 1 kHz. The 365–368-nm excitation needed for  $7s\ 2S_{1/2} \rightarrow 9p\ 2P_{1/2,3/2}$  was produced by a second Ti:Sa laser by internal cavity SHG. The 342–343-nm excitation step for  $7s\ 2S_{1/2} \rightarrow 10p\ 2P_{1/2,3/2}$  was generated by an optical parametric oscillator (OPO), at 100-Hz repetition rate. The 1064-nm ionization step was provided by a Nd:YAG laser for all schemes. For lifetime studies, the excitation step was produced by the OPO for all energy levels. All lasers were operated pulsed and in broadband configuration, with linewidths  $\Delta\nu \sim 3\ \text{GHz}$  for the two Ti:Sa, and  $\sim 200\ \text{GHz}$  for the OPO. As a stable frequency reference, a diode laser was frequency-stabilized using saturated absorption spectroscopy on the  $5s\ 2S_{1/2}\ F = 2 \rightarrow 5p\ 2P_{1/2}\ F' = 1$  hyperfine transition in  $^{87}\text{Rb}$ , referenced at  $12578.84851\ \text{cm}^{-1}$  [24]. The frequency of the OPO laser was determined via an internal reference calibrated on known atomic lines in francium and rubidium (see Supplemental Material). The Ti:Sa laser pulses at 422 nm had a full width at half maximum (FWHM) of 46(3) ns with a jitter of 5 ns, while the 365–368-nm Ti:Sa pulses had a FWHM of 38(2) ns and a 4-ns jitter. The OPO laser produced pulses with a FWHM of 2.2(1) ns and a jitter of 0.07 ns, and the Nd:YAG laser pulses had a FWHM of 10(2) ns with 0.5-ns jitter. Laser pulse timing was controlled using an ultra-low-jitter ( $< 50\ \text{ps}$ ) multi-channel signal generator.

Examples of the resonance ionization spectra of  $^{221}\text{Fr}$  are shown in Fig. 2. The amplitude of the signal is shown as a function of the rest frame wavenumber of the transition. The data were binned in frequency such that each spectral peak was sampled by at least 8–10 bins across its FWHM. The statistical uncertainty associated with each data point was taken as the square root of the total number of counts in each bin. For each dataset, the centroid value and uncertainty estimates were extracted

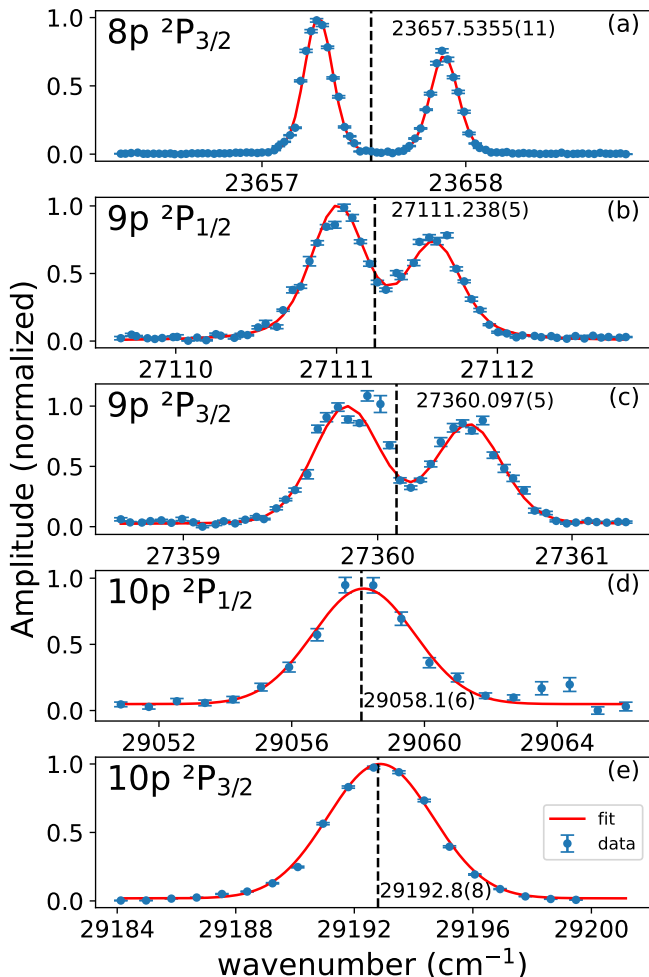


FIG. 2: Measured spectra for  $^{221}\text{Fr}$  transitions. The upper-level hyperfine splittings are unresolved. For (a), (b) and (c) the two-peak structure is dominated by the hyperfine splitting in the ground state  $7s^2S_{1/2}$ . For (d) and (e) the laser linewidth is too large to resolve it. The centroid is indicated by a vertical dashed black line with its value labelled.

using a least-squares fit with the SATLAS package [25].

For the reference level  $8p^2P_{3/2}$ , the ratio  $A(8p^2P_{3/2})/A(7s^2S_{1/2}) = 0.0036$  was constrained [26]. Due to the limited laser resolution, the hyperfine structure of the upper level was not resolved, and the separation between its hyperfine components is small compared to the observed linewidth [27]. Fixing the ratio allows a reliable determination of the ground-state magnetic-dipole hyperfine coefficient, yielding  $A(7s^2S_{1/2}) = 6200(16)$  MHz, in agreement with the literature value obtained from high-precision measurements performed within our group using the same experimental setup [28].

The value of  $A(7s^2S_{1/2})$  was then kept fixed in the fits used to extract the centroids of the transitions to the 9p

and 10p doublets. For these higher-lying states, the hyperfine splittings are even smaller relative to the experimental linewidth, and the ratios between ground- and excited-state hyperfine coefficients are not known. The  $A$  and  $B$  hyperfine coefficients of the upper states, as well as the Gaussian and Lorentzian widths, were kept as free parameters in the fits. Fixing the well-characterized ground-state coefficient proved necessary for stable centroid extraction.

We summarize all our results in Table I. The centroid of the  $7s^2S_{1/2} \rightarrow 8p^2P_{3/2}$  transition for  $^{212}\text{Fr}$  and isotope shift between  $^{212}\text{Fr}$  and  $^{221}\text{Fr}$  have been previously measured, corresponding to a transition wavenumber of  $23657.529(5)$   $\text{cm}^{-1}$  for  $^{221}\text{Fr}$  [26]. Our value of  $23657.5355(11)$   $\text{cm}^{-1}$  is in agreement with this literature value within uncertainties.

For the wavenumber measurements, the main contribution to the total uncertainty is statistical in nature (which enables centroid determination to about 1/20th of the experimental linewidth), followed by the OPO wavenumber calibration in the case of the 10p levels, introducing a systematic uncertainty. Other factors, such as beam energy calibration and magnetic field effects, contribute far less significantly (see Tab. III. Supplemental Material Tab.)

We compared our experimental data to theoretical results obtained using the RCCSDT (Relativistic Coupled-Cluster with Single, Double, and Triple excitations) method. This framework provides a consistent treatment of electron correlations. In the experiment, we measured the absolute energy difference between the  $7s^2S_{1/2}$  ground state and an excited state, whereas the *ab initio* calculations provide valence-electron binding (removal) energies referenced to the ionization potential. To enable a direct comparison, the  $7s^2S_{1/2}$  ground-state binding energy was calculated, yielding  $23811.67(13)$   $\text{cm}^{-1}$ , which differs from the reference value reported in [14] by  $154$   $\text{cm}^{-1}$ . Contributions to this discrepancy include missing higher-order correlation effects, including quadruple excitations and contributions from high-angular-momentum orbitals, which require more computational capacity than currently available. To facilitate direct comparison with experimental excitation energies, we adjusted the  $7s$  energy so that the theoretical  $7s \rightarrow 8p$  transition matches the experimental value, and all other excitation energies are then reported relative to this adjusted ground state. The remaining discrepancies, which scatter less than  $5$   $\text{cm}^{-1}$ , can then be explained by smaller effects not fully captured in the present treatment, such as residual higher-order correlations, finite-basis limitations, or QED contributions.

Having established the comparison between theoretical and experimental excitation energies, we next turn to the measurement of radiative lifetimes, which provides a test of the accuracy of the calculated electric-dipole

TABLE I: Measured and calculated absolute wavenumbers and radiative lifetimes for  $^{221}\text{Fr}$ .

Level	Wavenumber ( $\text{cm}^{-1}$ )		Lifetime (ns)	
	Theory	Experiment	Theory	Experiment
$8p\ ^2P_{3/2}$	-	23657.5355(11) <sup>a</sup>	80.5(2.9) <sup>a</sup>	81.1(1.7) <sup>a</sup>
	23658.306 <sup>f</sup>	23657.529(5) <sup>g</sup>	81.4 <sup>b</sup>	83.5(1.5) <sup>e</sup>
			81.8(2.3) <sup>c</sup>	
			61.13 <sup>d</sup>	
$9p\ ^2P_{1/2}$	27116(13) <sup>a</sup>	27111.238(5) <sup>a</sup>	318(9) <sup>a</sup>	329(6)[2] <sup>a</sup>
	27118.21 <sup>f</sup>		319(10) <sup>c</sup>	
			233.4 <sup>d</sup>	
$9p\ ^2P_{3/2}$	27365(12) <sup>a</sup>	27360.097(5) <sup>a</sup>	186(6) <sup>a</sup>	179(5)[3] <sup>a</sup>
	27366.20 <sup>f</sup>		186(2) <sup>c</sup>	
			130.7 <sup>d</sup>	
$10p\ ^2P_{1/2}$	29060(12) <sup>a</sup>	29058.1(6)[8] <sup>a</sup>	574(4) <sup>a</sup>	553(21)[8] <sup>a</sup>
	29064.18 <sup>f</sup>		566(7) <sup>c</sup>	
			424.3 <sup>d</sup>	
$10p\ ^2P_{3/2}$	29195(11) <sup>a</sup>	29192.8(8)[8] <sup>a</sup>	356(5) <sup>a</sup>	362(5)[3] <sup>a</sup>
	29198.09 <sup>f</sup>		346(5) <sup>c</sup>	
			231.3 <sup>d</sup>	

Refs. <sup>a</sup>This work; <sup>b</sup>Estimated using the E1 matrix elements from [29]; <sup>c</sup>[30]; <sup>d</sup>[17]; <sup>e</sup>[31]; <sup>f</sup>[14, 15]; <sup>g</sup>Data from [26] corrected with an estimated isotope shift. ( ) statistical; [ ] systematic uncertainties, given when significant. See Supplemental Material Table I.

(E1) matrix elements. All lifetime measurements were performed using a two-step laser scheme. First using the OPO laser to excite the atom to the desired state, and the Nd:YAG laser to ionize the atom. To determine the lifetimes of the different levels, we recorded the average countrate on the ion detector over a 120-second period for several different delays between the two laser pulses. The optimal ISCOOL trap ejection timing was determined by maximizing the signal rate, thus optimizing the spatial and temporal overlap between the atomic bunch and the laser pulses. Lifetime measurements were taken for the optimal ejection timing, and  $\pm 1\ \mu\text{s}$  compared to optimal, to constrain potential systematic effects related to the ejection timing.

For each data point, the statistical uncertainty was taken as the square root of the total number of ions detected over the measurement period. The systematic uncertainty on the signal rate was estimated by taking reference points at zero delay between the first and second excitation step every five measurements, to monitor fluctuations in the atomic beam and laser parameters. Time scale uncertainties for delays are the pulse-to-pulse timing instability (jitter) of the lasers, determined as 0.5 ns.

The initially excited level does not decay strictly to the ground state but to lower-lying states, predominantly via allowed E1 transitions. As the 1064 nm laser can ionize states above  $23450\ \text{cm}^{-1}$ , the total measured signal is the sum of the population of the initial excited nP level, the contributions of states in the radiative decay cascade,

and a constant background

$$N_{\text{total}}(t) = N_a(t) + \sum_j N_j(t) + C,$$

where  $N_a(t)$  is the population of the initial level,  $N_j(t)$  are the cascade contributions and  $C$  is the background.

The upper-level population decays exponentially

$$N_a(t) = N_0 e^{-t/\tau_a}, \quad (1)$$

while we model the contribution of the lower-lying levels  $j$  as

$$N_j(t) = N_0 \text{BR}_{a \rightarrow j} \frac{\tau_j}{\tau_a - \tau_j} \left( e^{-t/\tau_a} - e^{-t/\tau_j} \right), \quad (2)$$

where  $\tau_a$  and  $\tau_j$  are the lifetimes of the upper and lower levels, respectively,  $N_0$  the initial population, and  $\text{BR}_{a \rightarrow j}$  is the branching ratio from  $a$  to  $j$ . In doing so, we assume that the ionization cross section from all atomic states is the same. We only consider direct feeding of state  $j$  from the nP state of interest, and neglect feeding of  $j$  through another state  $j'$ , as these feedings are strongly suppressed by the branching ratios, which favour decays to states below the ionization threshold. Their inclusion does not affect the extracted upper-level lifetime within the experimental uncertainty. The inclusion of cascade contributions results in a modest but consistent improvement in fit quality, reducing the reduced  $\chi^2$  by approximately 0.15 on average compared to a simple exponential decay model. We obtained the branching ratio by calculating

the transition probability for a specific decay channel and dividing it by the total transition probability from that excited state to all possible lower states (see Supplemental Materials). Note that this cascade model does not add any additional fit parameters compared to a simple exponential fit.

The background level was independently measured prior to the lifetime analysis. In the fitting procedure, the background contribution  $C$  was treated as a free parameter constrained within the range defined by the measured background mean  $\pm$  one standard deviation. This approach incorporates the experimental uncertainty of the background while preventing unphysical values.

The uncertainty was taken as the standard error  $\sigma = (\sum_i 1/\sigma_i^2)^{-1/2}$ , increased by  $\sqrt{\chi_p^2}$  when the reduced chi-squared exceeded unity. This adjustment avoids underestimation of uncertainties while preventing unnecessary deflation when the data are consistent. In addition, the uncertainties associated with the cascade parameters, namely the lifetimes  $\tau_j$  in Eq. 2, were propagated through the full model and included as a systematic contribution. To exclude data points where the laser pulses overlap, which would lead to deviations from the simple decay law, the initial 15 ns of the decay curve were omitted from the fits. This interval, referred to as the “laser overlap regime” in previous work [32], corresponds approximately to the sum of the lasers FWHM and their relative timing jitter. Typical curve is shown in Fig. 3 (all decay curves are shown in the Supplemental Material); no systematic deviations are seen for small decay times, confirming the validity of the chosen delay timings.

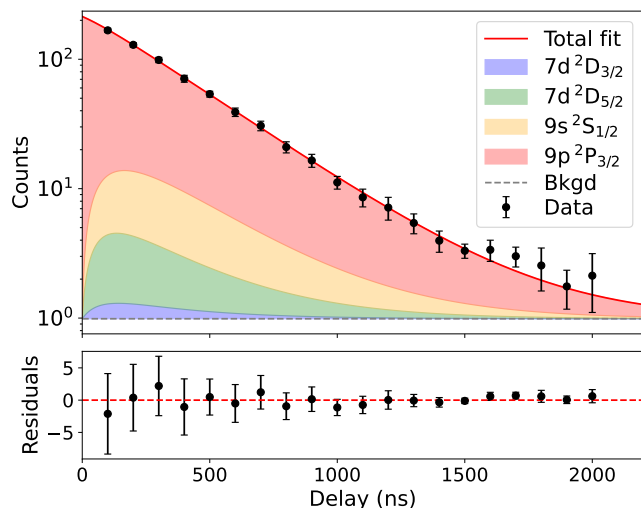


FIG. 3: Typical decay curves for the  $9p\ 2P_{3/2}$  level. The vertical axis uncertainties account for both statistics and systematics. The contributions of the ionized cascade levels are shown in different colors.

To assess the reliability of the experimental technique

and analysis method, the lifetime of the  $8p\ 2P_{3/2}$  level was measured using the same procedure and compared to the value reported in the literature [33]. Measurements 1–4 were recorded in the 2023 experimental campaign where they also served as reference for RaF lifetime measurements (details in [32]). Measurements 5–7 are from the 2024 campaign. The results, presented in Fig. 4, give a weighted mean of 81.1(1.7) ns, which is consistent with the literature value of 83.5(1.5) ns [33]. Measured lifetimes are compiled in Table I.

For the lifetime measurements, the dominant contribution to the systematic uncertainty arises from the lifetimes of lower-lying cascade levels,  $\tau_j$ , which were previously measured, including uncertainties (see Supplemental Materials). Because the initially excited level decays not only to the ground state but also populates these intermediate states according to the branching ratios  $BR_{a \rightarrow j}$ , the measured ion signal includes both the direct decay of the upper level,  $N_a(t)$ , and the cascade contributions,  $N_j(t)$ , as in Eq. (2). Uncertainties in the  $\tau_j$  values propagate into the total signal and thereby affect the fitted upper-level lifetime  $\tau_a$ . This effect is accounted for by individually varying each  $\tau_j$  within its reported uncertainty and refitting the decay curves; the resulting spread in  $\tau_a$  is treated as a systematic contribution. In addition, fluctuations in the laser-induced ion rate, which reflect variations in the overall RIS efficiency and the incoming ion flux, contribute further to the total uncertainty. The RIS efficiency itself depends on several experimental factors, including the laser ionization probability, the neutralization efficiency of the atomic beam, transport losses in the neutral and ion beams, and the ion detector efficiency. Variations in any of these parameters lead to changes in the measured signal counts, thereby affecting the decay curve data and ultimately the precision of the fitted lifetimes.

After obtaining experimental values, we performed RCC calculations of the electric dipole (E1) matrix elements in order to compare theory with experiment and evaluate the accuracy of the theoretical model, see Table I. The comparison between experimental and theoretical lifetimes shows good agreement within uncertainties for all states: the  $9p$  and  $10p$  levels exhibit relative deviations of 4% or less, with the largest deviation observed for the  $9p\ 2P_{3/2}$  state and the smallest for  $10p\ 2P_{3/2}$ . Discrepancies may result from incomplete treatment of electron correlation and the extended spatial distribution of high-lying Rydberg orbitals. Coupled-cluster calculations of alkali-metal atoms have shown that high-lying states are sensitive to the spatial extent of the wavefunctions and electron correlation, which standard coupled-cluster calculations may not fully capture [34, 35]. The good agreement indicates that the RCCSDT method yields accurate E1 matrix elements, which can be very useful for atomic parity violation studies using francium atoms [6, 7].

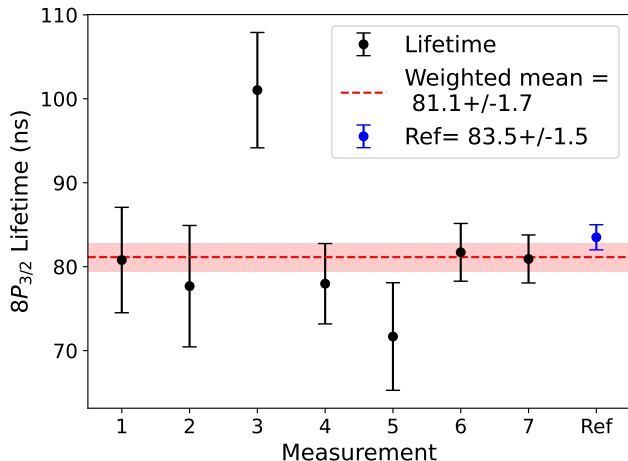


FIG. 4: Lifetime results for the  $8p^2P_{3/2}$  level. The red line and green shaded band indicate the error-weighted mean and one standard deviation calculated across all measurements. Ref from [33].

Two complementary conclusions can be drawn. First, while the RCCSDT calculations exhibit a systematic offset in the absolute binding energies, the relative excitation energies are reproduced with high accuracy. This indicates that the dominant missing contributions, such as higher-order excitations beyond triples, contributions from high-angular-momentum orbitals, and QED effects enter primarily as an approximately state-independent shift to the valence removal energy. The accurate reproduction of relative level spacings therefore demonstrates that the RCCSDT method captures the essential state-dependent correlation physics in francium.

Second, the agreement between calculated and measured lifetimes of all measured states provides an independent and more stringent validation of the theoretical wavefunctions. Since excited-state lifetimes are directly determined by electric-dipole (E1) transition matrix elements, this agreement indicates that the RCCSDT approach yields highly-accurate E1 matrix elements. Together, these results confirm that relativistic coupled-cluster theory at the RCCSDT level provides a reliable and internally-consistent description of both the atomic energy structure and transition properties of francium, supporting its use in precision spectroscopy and atomic parity-violation studies. Future work will include results from ongoing measurements of the higher members of the P series as well as the 6d and higher angular momentum states, while a more precise determination of isotope shifts remains an important goal. Such measurements will not only complete the spectroscopic picture of francium but also provide essential input data for tests of fundamental symmetries.

*Acknowledgements* We thank the ISOLDE techni-




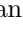





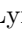






cal teams for their support. We also acknowledge funding and support from the following sources : KU Leuven BOF (No. C14/22/104), EOS project MANASLU (No. 40007501), FWO grant (No. G0F7321N), EURO-LABS project (No. 101057511) and STFC Grants No. ST/Y000323/1, ST/X00502X/1, and ST/V001116/1. K.M.L. acknowledges support from the Royal Society Grant No. DHF /R1/231007 and UK Research and Innovation (UKRI) under the UK government’s Horizon Europe funding Guarantee Grant No. EP/Y036816/1 (ESPEN).

---

\* Corresponding author: pierre.lassegues@cern.ch

- [1] X. C. Vidal, M. D’Onofrio, P. J. Fox, R. Torre, K. A. Ulmer, A. Aboubrahim, A. Albert, J. Alimena, B. C. Allanach, *et al.*, Beyond the standard model physics at the hl-lhc and he-lhc (2019).
- [2] M. R. Tarbutt, J. J. Hudson, B. E. Sauer, and E. A. Hinds, *Faraday Discussions* **142**, 37 (2009).
- [3] Y. Sakemi, K. Harada, T. Hayamizu, M. Itoh, H. Kawamura, S. Liu, H. S. Nataraj, A. Oikawa, *et al.*, *J. Phys.: Conf. Ser.* **302** (2011).
- [4] S. Aubin, J. Behr, R. Collister, V. Flambaum, E. Gomez, G. Gwinner, K. Jackson, *et al.*, *Hyperfine Interact* **214**, 163 (2013).
- [5] E. Gomez, S. Aubin, G. D. Sprouse, L. A. Orozco, and D. P. DeMille, *Phys. Rev. A* **75**, 033418 (2007).
- [6] T. Aoki, Y. Torii, B. Sahoo, B. Das, K. Harada, T. Hayamizu, K. Sakamoto, H. Kawamura, T. Inoue, A. Uchiyama, *et al.*, *Appl. Phys. B*, 509 (2018).
- [7] A. Kastberg, T. Aoki, B. Sahoo, Y. Sakemi, and B. Das, *Physical Review A* **100**, 050101 (2019).
- [8] E. Gomez, S. Aubin, R. Collister, J. A. Behr, G. Gwinner, L. A. Orozco, M. R. Pearson, M. Tandecki, D. Sheng, and J. Zhang, *J. Phys. Conf. Ser.* **387**, 012004 (2012).
- [9] W. Z. Zhao, J. E. Simsarian, L. A. Orozco, W. Shi, and G. D. Sprouse, *Phys. Rev. Lett.* **78**, 4169 (1997).
- [10] U. I. Safronova, W. R. Johnson, and M. S. Safronova, *Phys. Rev. A* **76**, 042504 (2007).
- [11] B. K. Sahoo, D. K. Nandy, B. P. Das, and Y. Sakemi, *Phys. Rev. A* **91**, 042507 (2015).
- [12] M. Vajed-Samii, J. Andriessen, B. P. Das, S. N. Ray, T. Lee, and T. P. Das, *Phys. Rev. Lett.* **49**, 1800 (1982).
- [13] A. Owusu, R. W. Dougherty, G. Gowri, T. P. Das, and J. Andriessen, *Phys. Rev. A* **56**, 305 (1997).
- [14] A. Kramida, Y. Ralchenko, J. Reader, and NIST ASD Team, *NIST Atomic Spectra Database* (2024).
- [15] E. Biémont, P. Quinet, and V. Van Renterghem, *J. Phys. B: At. Mol. Opt. Phys.* **31**, 5301 (1998).
- [16] M. Das and A. C. Pradhan, *J. Phys. B: At. Mol. Opt. Phys.* **52**, 155001 (2019).
- [17] W. Van Wijngaarden and J. Xia, *J. Quant. Spec. Rad. Tr.* **61**, 557 (1999).
- [18] E. Kugler, *Nucl. Instrum. Methods Phys. Res. B* **79**, 322 (1993).
- [19] R. Catherall, W. Andreatza, M. Breitenfeldt, A. Dorsival, G. J. Focker, T. P. Gharsa, T. J. Giles, J.-L. Grenard, *et al.*, *J. Phys. G: Nucl. Part. Phys.* **44**, 094002 (2017).
- [20] T. J. Giles, R. Catherall, V. Fedosseev, U. Georg, E. Kugler, J. Lettry, and M. Lindroos, *Nucl. Instrum. Methods Phys. Res. Sect. B* **204**, 497 (2003).
- [21] E. Mané, J. Billowes, K. Blaum, P. Campbell, B. Cheal, P. Delahaye, K. T. Flanagan, D. H. Forest, H. Franberg, C. Geppert, *et al.*, *Eur. Phys. J. A* **42**, 503 (2009).
- [22] A. Koszorus, J. Billowes, C. L. Binnersley, M. L. Bissell, T. E. Cocolios, B. S. Cooper, R. P. de Groote, G. Farooq-Smith, V. N. Fedosseev, K. T. Flanagan, *et al.*, *Nucl. Instrum. Methods Phys. Res. B* **463**, 398 (2020).
- [23] A. R. Vernon, R. P. de Groote, J. Billowes, C. L. Binnersley, T. E. Cocolios, G. J. Farooq-Smith, K. T. Flanagan, R. F. Garcia Ruiz, W. Gins, *et al.*, *Nucl. Instrum. Methods Phys. Res. B* **463**, 384 (2020).
- [24] D. A. Steck, Rubidium 87 d line data (2001).
- [25] W. Gins, R. P. de Groote, M. L. Bissell, C. Granados Buitrago, R. Ferrer, K. M. Lynch, G. Neyens, and S. Sels, *Comp. Phys. Comm.* **222**, 286 (2018).
- [26] H. Duong, P. Juncar, S. Liberman, A. Mueller, R. Neugart, E. Otten, B. Peuse, J. Pinard, H. Stroke, C. Thibault, and others, *EPL* **3**, 175 (1987).
- [27] J. E. Sansonetti, *J. Phys. Chem. Ref. Data* **36**, 497 (2007).
- [28] I. Budincević, J. Billowes, M. Bissell, T. E. Cocolios, R. P. De Groote, S. De Schepper, V. N. Fedosseev, K. T. Flanagan, S. Franchoo, R. G. Ruiz, and others, *Phys. Rev. C* **90**, 014317 (2014).
- [29] B. Roberts, C. Fairhall, and J. Ginges, *Phys. Rev. A* **107**, 052812 (2023).
- [30] Y.-B. Tang, B.-Q. Lou, and T.-Y. Shi, *Phys. Rev. A* **96**, 022513 (2017).
- [31] S. Aubin, E. Gomez, L. Orozco, and G. Sprouse, *Phys. Rev. A* **70**, 042504 (2004).
- [32] M. Athanasakis-Kaklamanakis, S. G. Wilkins, P. Lassègues, L. Lalanne, J. R. Reilly, O. Ahmad, M. Au, S. W. Bai, J. Berbalk, *et al.*, *Phys. Rev. A* **110**, L010802 (2024).
- [33] S. Aubin, E. Gomez, L. A. Orozco, and G. D. Sprouse, *Phys. Rev. A* **70**, 042504 (2004).
- [34] R. Pal, M. S. Safronova, W. R. Johnson, A. Derevianko, and S. G. Porsev, *Phys. Rev. A* **75**, 042515 (2007).
- [35] M. S. Safronova and U. I. Safronova, *Phys. Rev. A* **83**, 052508 (2011).

# Energies and lifetimes of the 9p and 10p excited states in atomic francium

P. Lassègues <sup>1,\*</sup> A. Ajayakumar,<sup>2</sup> M. Athanasakis-Kaklamanakis <sup>3</sup> O. Ahmad,<sup>1</sup> M. Au <sup>2,4</sup> J. Berbalk,<sup>1,2</sup> D. Bettaney,<sup>5</sup> B. van den Borne <sup>1</sup> A. Chakraborty <sup>6</sup> T.E. Cocolios <sup>1</sup> M. Duggan,<sup>5</sup> C. Fajardo <sup>1,7</sup> K.T. Flanagan <sup>5</sup> R.F. Garcia Ruiz,<sup>8,9</sup> R. de Groote <sup>1</sup> D. Gonzalez-Acevedo,<sup>8</sup> A. Kastberg,<sup>10</sup> A. Koszorús,<sup>1</sup> L. Lalanne,<sup>11</sup> K.M. Lynch <sup>5</sup> D.T. McLeroy,<sup>5</sup> A. McGlone <sup>5</sup> G. Neyens <sup>1</sup> L. Nies <sup>7</sup> L. Quanjel,<sup>1,12</sup> A. Raggio <sup>1</sup> J. Reilly,<sup>5</sup> B.K. Sahoo <sup>6</sup> J. Snikeris,<sup>13,14</sup> J. Warbinek,<sup>7</sup> S.G. Wilkins,<sup>8</sup> and X.F. Yang <sup>15</sup>

<sup>1</sup>*KU Leuven, Instituut voor Kern-en Stralingsfysica, 3001, Leuven, Belgium*

<sup>2</sup>*Systems Department, CERN, CH-1211 Geneva 23, Switzerland*

<sup>3</sup>*JILA and University of Colorado, Boulder, Colorado 80309, USA*

<sup>4</sup>*Department of Chemistry, Johannes Gutenberg-Universität Mainz, 55099 Mainz, Germany*

<sup>5</sup>*Department of Physics and Astronomy, The University of Manchester, Manchester M13 9PL, United Kingdom*

<sup>6</sup>*Physical Research Laboratory, Ahmedabad-380009, India*

<sup>7</sup>*Experimental Physics Department, CERN, CH-1211 Geneva 23, Switzerland*

<sup>8</sup>*Department of Physics, Massachusetts Institute of Technology, Cambridge, Massachusetts 02139, USA*

<sup>9</sup>*Laboratory for Nuclear Science, Massachusetts Institute of Technology, Cambridge, Massachusetts 02139, USA*

<sup>10</sup>*Institut de Physique de Nice, Université Côte d'Azur, 06108 Nice, France*

<sup>11</sup>*Université Paris-Saclay, CNRS/IN2P3, IJCLab, Orsay, F-91405, France*

<sup>12</sup>*Belgian Nuclear Research Centre, SCK CEN, 2400 Mol, Belgium*

<sup>13</sup>*Department of Physics, University of Gothenburg, 412 96 Gothenburg, Sweden*

<sup>14</sup>*Institute of Atomic Physics and Spectroscopy, University of Latvia, 1004 Riga, Latvia*

<sup>15</sup>*School of Physics and State Key Laboratory of Nuclear Physics and Technology, Peking University, Beijing, China*

(Dated: May 13, 2026)

## SUPPLEMENTAL MATERIAL

### Uncertainty Analysis

The uncertainty analysis shows that the energy and lifetime measurements are dominated by different primary sources of uncertainty. For the energy (wavenumber) measurements, the statistical uncertainty is mainly governed by the laser linewidth, which limits the resolvability of the hyperfine components and consequently degrades the precision of the hyperfine-structure fitting procedure. Followed by a systematic contribution from the OPO wavenumber calibration for the 10p levels. In contrast, the lifetime measurements are primarily limited by the uncertainties of the lifetimes of lower-lying cascade levels, which were propagated through the full model as a systematic contribution. In addition, fluctuations in the laser-induced ion rate, reflecting variations in the overall resonance ionization efficiency and beam intensity, also contribute to the uncertainty. The following paragraphs provide a detailed discussion of the individual uncertainty contributions and the methods used to estimate them.

*Charge exchange effects* An uncertainty can be attributed to the charge exchange process, arising from the population of intermediate excited states during neutralization. These states decay to the observed states with additional kinetic energy, causing Doppler-shifted side peaks (approximately 40 MHz detuned) [1]. Their contribution, especially when enhanced by inelastic collisions with sodium vapor can distort the lineshape and shift the fitted resonance. However, no measurable ef-

fect attributable to this mechanism has been observed for francium [3].

*Ion beam gate* The ion beam is gated using a pulsed extraction electrode located at the end of ISCOOL, which is driven with a fast voltage pulse of approximately 50 V to open and close the trap and release the ion bunch. This ion beam gate defines the extraction timing and initial acceleration conditions of the ions. In practice, residual potentials on the order of 1–2 V can remain during the extraction process. These residual electric fields modify the effective extraction potential experienced by the ions, leading to shot-to-shot variations in their longitudinal velocity. Such velocity variations translate into fluctuations of the Doppler shift in the collinear laser–ion interaction, which in turn increase the uncertainty of the fitted spectral line centroid.

*Beam-laser angle misalignment* To estimate the systematic frequency shift due to beam misalignment, we consider a small angular deviation between the ion and laser beams. The ion velocity is calculated classically as  $v = \sqrt{2E/m}$ , giving  $\beta = v/c \approx 5.398 \times 10^{-4}$  and the Lorentz factor  $\gamma \approx 1.00000015$ . A lateral displacement of 1 cm over a 2.36 m propagation path, taken as a conservative estimate of the beam misalignment, corresponds to an angular deviation of  $\theta \approx \arctan(0.01/2.36) = 4.237$  mrad. Using the small-angle approximation  $\cos(\theta) \approx 1 - \theta^2/2$ , the relativistic Doppler shift for an angle  $\theta$  between the laser and ion beams is approximated by:

$$\Delta\nu \approx \nu_0 \gamma \beta \left( -\frac{\theta^2}{2} \right)$$

TABLE I: Summary of uncertainties in frequency and lifetime measurements. \* dataset-specific

Source	Estimated Uncertainty	Notes
<b>Beam-Related Uncertainties</b>		
Beam energy calibration	$\pm 4$ MHz	Based on readout and known fluctuation ( $\pm 0.6$ eV)
Ion beam switch	$\pm 3$ MHz	1% uncertainty on a 50 V gate
Beam-laser angle misalignment	$-3$ MHz	1 cm conservative lateral offset $\rightarrow$ Doppler error
Charge exchange effects	Negligible for Fr	Doppler-shifted sidepeaks from excited states [1]
<b>Laser-Related Errors</b>		
Wavemeter accuracy	$\pm 2$ MHz	Technical specification
Laser frequency drift	Negligible	Compared and corrected using absolute reference lines
OPO frequency calibration	$\pm 24$ GHz	Calibrated using reference lines and previous measurement
AC Stark shift	$< 1$ MHz	Delayed high-power ionization pulse [2]
<b>Other Frequency Errors</b>		
Zeeman shift	$< 1$ MHz	Ambient field $\sim 5-10 \times 10^{-5}$ T, no observed broadening
Residual stray fields	Negligible	Within sensitivity, no stray electric fields were detected.
<b>Lifetime Measurement</b>		
Cascade level lifetimes	$\pm 2-8$ ns *	Lower-state uncertainties propagate through cascade fit
Laser timing jitter	$\pm 0.07$ ns (OPO) $\pm 0.49$ ns (Nd:YAG)	Std. dev. of pulse centroids (FWHM: 2.2 ns, 10 ns)
$t_0$ offset (Laser-DAQ sync)	$< 1$ ns	Extracted from timing reference pulses
Beam intensity fluctuations	$\pm 0, 5-5\%*$	Zero-delay references to account for beam fluctuations
Laser-ion signal fluctuations	$\pm 1-15\%*$	Statistical uncertainty from integrated counts
Experimental background	$\pm 0, 3-4\%*$	Extracted from gate-closed, laser-off, and laser-detuned data

For a transition wavelength of 422 nm ( $\nu_0 = c/\lambda \approx 7.10 \times 10^{14}$  Hz), the resulting systematic frequency shift is  $\Delta\nu \approx -3.44$  MHz.

*-OPO frequency calibration* For the wavenumber measurement of the 10p doublet we used the OPO laser. In contrast to the Ti:Sa lasers used for the other levels, it could not be compared to the reference line in  $^{87}\text{Rb}$ , since the linewidth of the OPO laser ( $\sim 200$  GHz) is too large to be read accurately by the wavemeter. To calibrate the data, we directly measured the  $8p^2P_{3/2}$  and  $9p^2P_{1/2,3/2}$  lines in  $^{221}\text{Fr}$ , as well as  $7p^2P_{1/2}$  and  $8p^2P_{1/2,3/2}$  in  $^{87}\text{Rb}$  also with the OPO laser. Thus we obtained comparisons to the data taken with Ti:Sa lasers and the wavemeter and to [4]. This is illustrated in Fig. 1. The calibrated reference frequency is determined from the fit equation  $y = mx + k = 0.999707(1)x - 1.47(2)$ . We propagate the uncertainties from  $m$ ,  $k$ , and the measured value  $x$ . This gives an uncertainty of  $0.7887 \text{ cm}^{-1}$ , equivalent to approximately 23.66 GHz.

*-Laser Pulses characterization* Before the experiment, the timing characteristics of each laser (OPO and Nd:YAG) used for the lifetime measurements were recorded using a Lecroy WavePro 7 Zi oscilloscope and two silicon photodiode detectors, to extract both the pulse shapes and their shot-to-shot stability (jitter). These detectors, each aligned to monitor a separate laser beam, were positioned on the laser table ahead of the beamline, with signal levels kept below saturation. The oscilloscope was externally triggered by a low-jitter ( $< 50$  ps) Quantum Composers 9520 Pulse Generator. To characterize the pulse shape, we recorded 1000 consecu-

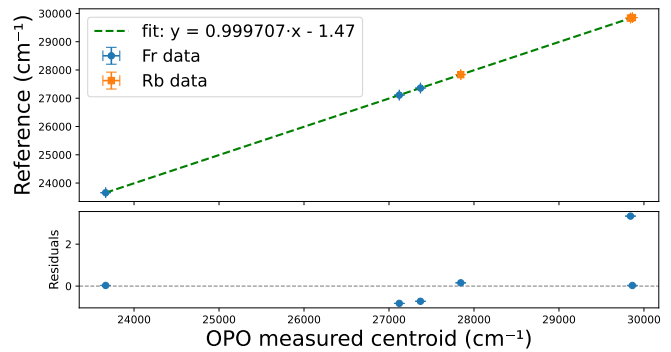
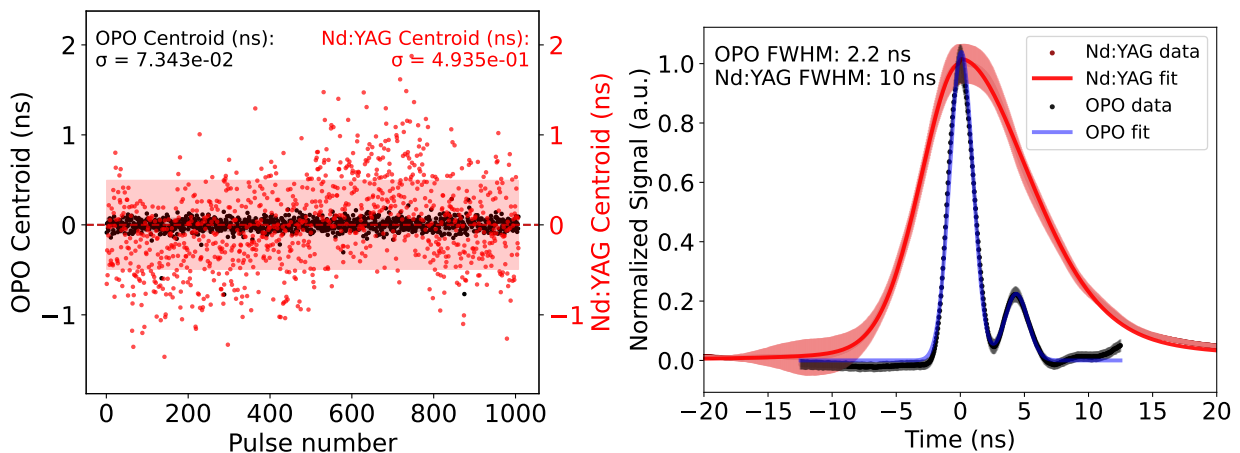


FIG. 1: Calibration curve for the OPO laser, based on known reference transitions in  $^{221}\text{Fr}$  and  $^{87}\text{Rb}$ , used to calibrate the frequency for the 10p measurements.

tive pulses for both lasers. The resulting waveforms were averaged, providing timing profiles. These profiles (Fig. 2) were then fitted with a skewed Voigt profile, to extract the full-width at half-maximum (FWHM), 2.2 ns for the OPO and 10 ns for the Nd:YAG at the centroid. The timing jitter was determined as the standard deviation of the centroid distribution, with a value of 0.07 ns for the OPO and 0.49 ns for the Nd:YAG.

*-Experimental background* For each lifetime measurement, the background signal was characterized under several distinct experimental conditions: with the ion beam blocked, with all lasers off, with only the excitation laser on, with only the ionization laser on, and with both lasers on but far detuned from any resonance. In each case, the background level was extracted by tak-



(a) Shot-to-shot fluctuations: Centroid positions of each pulse relative to the mean, with standard deviation shown for both lasers (surrounding band). OPO laser (black) and Nd:YAG laser (red).

(b) Averaged pulse shape over 1000 pulses with respective standard deviation on each point (surrounding band) for both lasers. OPO laser (black) and Nd:YAG laser (red). A reflection in the setup introduces a secondary peak in the OPO signal, which was not accounted for in the determination of the full width at half maximum (FWHM).

FIG. 2: Pulse timing profiles of the lasers and their pulse-to-pulse timing stability (jitter)

ing the average number of counts on the detector over the full-time window of the corresponding dataset. The total mean background was then reconstructed based on the contributions from these measurements. The mean components associated with the ion beam blocked and laser-off conditions were treated as linearly additive, as they originate from independent sources: residual background radiation in the beamline, dark counts on the ion detector, or noise on the electronic signal for the first one and collisional excitation processes for the second. In contrast, the laser-induced backgrounds (Nd:YAG, OPO, or both) were not assumed to be additive, due to potential non-linear dependencies in contributions to the effect. Since the lasers were detuned from any other known resonances, we attribute these backgrounds to non-resonant excitation processes, such as multiphoton effects. Under this assumption, the highest background level observed among the laser-on configurations was taken as a conservative upper bound for the laser-induced background in each measurement. Since the spatial overlap and alignment were individually optimized for each level measurement to maximize the signal, the efficiency and magnitude of laser-induced background contributions varied across datasets. Therefore, these components were treated independently in the analysis and fitted separately for each measurement condition. The total mean background  $\langle B_{\text{total}} \rangle$  can thus be expressed as

$$\langle B_{\text{total}} \rangle = \langle B_{\text{beamgate}} \rangle + \langle B_{\text{laseroff}} \rangle + \max(\langle B_{\text{Trili}} \rangle, \langle B_{\text{OPO}} \rangle).$$

To account for uncertainty in the background measurement, we treated the background level as a constrained

parameter in the exponential decay fit rather than fixing it *a priori*. The background was allowed to vary within the range defined by its experimental uncertainty, using the measured value as a prior estimate. This approach ensures proper uncertainty propagation, reduces bias in the decay parameters, and accounts for potential variations between background and signal acquisition conditions.

–*Cascade levels lifetimes* The systematic uncertainty arising from cascade feeding was evaluated by propagating the lifetimes of the lower-lying states. Since the total signal

$$N_{\text{tot}}(t) = N_a(t) + \sum_j N_j(t) + C, \quad (1)$$

depends explicitly on the cascade lifetimes  $\tau_j$ , uncertainties in these previously determined quantities influence the extracted upper-level lifetime  $\tau_a$ . In particular, through

$$N_j(t) = N_0 \text{BR}_{a \rightarrow j} \frac{\tau_j}{\tau_a - \tau_j} \left( e^{-t/\tau_a} - e^{-t/\tau_j} \right), \quad (2)$$

variations in  $\tau_j$  modify the time dependence of the cascade contribution and therefore the fitted value of  $\tau_a$ .

The propagation was evaluated numerically using a finite-difference approach. For each cascade level  $j$ , the lifetime was varied independently by  $\pm\sigma_{\tau_j}$ , and the decay curve was refitted to extract the corresponding values  $\tau_a^{(+)}$  and  $\tau_a^{(-)}$ . The sensitivity of the upper-level lifetime

to the parameter  $\tau_j$  was then estimated as

$$\Delta\tau_a^{(j)} = \frac{\tau_a^{(+)} - \tau_a^{(-)}}{2}, \quad (3)$$

which corresponds to the first-order propagation term

$$\Delta\tau_a^{(j)} \approx \left| \frac{\partial\tau_a}{\partial\tau_j} \right| \sigma_{\tau_j}. \quad (4)$$

Assuming independent cascade parameters, the total systematic uncertainty from cascade feeding was obtained by adding the individual contributions in quadrature,

$$\sigma_{\tau_a, \text{sys}}^2 = \sum_j \left( \Delta\tau_a^{(j)} \right)^2. \quad (5)$$

This systematic contribution was then combined in quadrature with the statistical uncertainty from the fit to obtain the total uncertainty on  $\tau_a$ .

### RCC calculations

To understand our results theoretically, we have calculated the measured quantities using the RCC theory [5, 6]. An atomic wave function of an atomic state with closed-core [6p<sup>6</sup>] and a valence orbital  $v$  of francium in the RCC theory framework can be expressed as

$$|\Psi_v\rangle = e^T \{1 + S_v\} |\Phi_v\rangle, \quad (6)$$

where  $|\Phi_v\rangle$  is the Dirac-Hartree-Fock (DHF) wave function,  $T$  is the RCC operator that accounts for the excitations of core electrons to the virtual orbitals, and  $S_v$  is responsible for exciting electron from the valence orbital correlating with core electrons to the virtual orbitals. For accurate calculations of the DHF wave functions of all the considered states of Fr, we have employed an extensive size basis-set of primitive Gaussian-type orbitals (GTOs). The basis-set consisted of 40, 39, 38, 37, 36, 35, and 34 GTOs for the s, p, d, f, g, h, and i symmetries, respectively.

The amplitude and energy ( $E_v$ ) determining equations of the RCC theory are given by

$$\langle \Phi^* | (\bar{H}_N - E_v) S_v + \bar{H}_N | \Phi_v \rangle = 0 \quad (7)$$

and

$$E_v = \langle \Phi_v | \bar{H}_N S_v + \bar{H}_N | \Phi_v \rangle \quad (8)$$

respectively. In the above expressions,  $|\Phi^*\rangle$  denotes an excited state determinant with respect to  $|\Phi_v\rangle$  and appropriately selected to evaluate amplitudes of the  $T$  and  $S_v$  operators.  $H_N$  is the normal-ordered atomic Hamiltonian. For convenience, this is defined with respect to the [6p<sup>6</sup>] configuration so that  $E_v$  directly corresponds

to the negative of the ionization potential of the valence electron. We start calculations with the Dirac-Coulomb approximation in the Hamiltonian, then corrections from the Breit and QED effects are added separately. Since both amplitude and  $E_v$  equations are interdependent, the above equations are solved simultaneously.

After obtaining wave functions of atomic states, matrix elements of the electric dipole (E1) operator,  $D$ , between two states described by wave functions  $|\Psi_f\rangle$  and  $|\Psi_i\rangle$  are evaluated as

$$\langle \Psi_f | D | \Psi_i \rangle = \frac{\langle \Phi_f | \{1 + S_f^\dagger\} \bar{D} \{1 + S_i\} | \Phi_i \rangle}{\sqrt{N_i N_f}}, \quad (9)$$

where  $N_{v=i,f} = \langle \Phi_v | \{1 + S_v^\dagger\} e^{T^\dagger} e^T \{1 + S_v\} | \Phi_v \rangle$  and  $\bar{D} = e^{T^\dagger} D e^T$ . The non-terminating series appearing in these expressions are accounted for by computing them through self-consistent procedures.

### Lifetime measurement details

The lifetime measurements were distributed over two beamtime campaigns. From the combined data, weighted means and uncertainty limits are derived. This is further accounted for in Tab. II. Decay curves for levels 9p<sup>2</sup>P<sub>1/2</sub>, 10p<sup>2</sup>P<sub>1/2</sub> and 10p<sup>2</sup>P<sub>3/2</sub> are shown in figures 3,4 and 5.

### Lifetimes and Branching ratios

The transition probability (in s<sup>-1</sup>) of an atomic state ( $|\Psi_i\rangle$ ) to a lower state ( $|\Psi_f\rangle$ ) due to the E1 decay channel is given by

$$A_{i \rightarrow f} = \frac{2.02613 \times 10^{15}}{(2J_i + 1) \lambda_{i \rightarrow f}^3} |\langle J_i || D || J_f \rangle|^2, \quad (10)$$

where  $\lambda_{i \rightarrow f}$  is the transition wavelength (in nm) and  $\langle J_i || D || J_f \rangle$  is the reduced E1 transition matrix element (in atomic units (a.u.)) with the angular momentum of the states as  $J$ . The lifetime (in s) of the state  $|\Psi_i\rangle$ , then, is determined by

$$\tau_i = \frac{1}{\sum_f A_{i \rightarrow f}}. \quad (11)$$

The branching ratios ( $BR$ ) for each state are listed in Table III. According to Eq. (10), the transition probability depends on the cube of the energy difference associated with the decay channel. As the principal quantum number  $n$  increases, the energy spacing between adjacent states becomes smaller. For any  $np^2P_{1/2}$  or  $np^2P_{3/2}$  state, the primary decay path is to the  $ns^2S_{1/2}$  state. However, at higher  $n$ , the energy gap between the  $np$  and  $ns$  levels decreases, leading to a reduced transition rate  $A$ , and thus longer lifetimes. This trend is also evident

TABLE II: Details of the different cycles in the lifetime measurement.  $8p^2P_{3/2}$  cycles 1–4 were previously reported in [7]. The systematic signal uncertainties correspond to the added uncertainty on the count rate, in order to account for atomic beam fluctuations.

Level	Step n°	ISCOOL ejection mod. delay( $\mu$ s)	Syst. signal uncert.(%)	Lifetime (ns)
$8p^2P_{3/2}$	1	Ion.	0	3.19
	2	Ion.	-0.5	3.1
	3	Ion.	+0.5	1.09
	4	Exc.	0	5.87
	5	Ion.	0	7.84
	6	Ion.	+1	1.18
	7	Ion.	-1	1.31
			wtd. mean:	<b>81.14(1.71)</b>
ref. [8]				83.5(1.5)
$9p^2P_{3/2}$	1	Ion.	0	0.98
	2	Ion.	+1	1.15
	3	Ion.	-1	0.99
				wtd. mean:
$9p^2P_{1/2}$	1	Ion.	0	1.94
	2	Ion.	+1	1.62
	3	Ion.	-1	1.09
			wtd. mean:	<b>329.36(5.59)</b>
$10p^2P_{3/2}$	1	Ion.	0	0.49
	2	Ion.	+1	0.55
	3	Ion.	-1	0.36
			wtd. mean:	<b>362.00(4.95)</b>
$10p^2P_{1/2}$	1	Ion.	0	1.99
	2	Ion.	+1	2.58
	3	Ion.	-1	1.91
			wtd. mean:	<b>553.32(20.48)</b>

from the  $BR$ s in Table III. Additionally, the E1 matrix element between high- $np$  states and lower  $ns$  states is relatively small; although the energy gap in these cases is larger, it does not significantly affect the lifetime of the corresponding  $P_{1/2}$  and  $P_{3/2}$  states. However, for the  $np^2P_{3/2}$  state, the matrix element with the  $7s^2S_{1/2}$  state is considerable, which leads to shorter lifetimes compared to its  $P_{1/2}$  counterparts. See also in Table IV the values of lifetimes used in the different cascade fit with their uncertainties.

TABLE III: E1 Decay channel and branching ratio of different  $np^2P_{1/2}$  and  $np^2P_{3/2}$  states of  $^{221}\text{Fr}$ .

State	Decay Channel	$BR$	State	Decay Channel	$BR$
$8p^2P_{3/2}$	$\rightarrow 7s^2S_{1/2}$	0.47			
	$\rightarrow 6d^2D_{3/2}$	0.01			
	$\rightarrow 6d^2D_{5/2}$	0.11			
	$\rightarrow 8s^2S_{1/2}$	0.42			
$9p^2P_{1/2}$	$\rightarrow 7s^2S_{1/2}$	0.07	$9p^2P_{3/2}$	$\rightarrow 7s^2S_{1/2}$	0.36
	$\rightarrow 6d^2D_{3/2}$	0.24		$\rightarrow 6d^2D_{3/2}$	0.01
	$\rightarrow 8s^2S_{1/2}$	0.12		$\rightarrow 6d^2D_{5/2}$	0.08
	$\rightarrow 7d^2D_{3/2}$	0.29		$\rightarrow 8s^2S_{1/2}$	0.21
	$\rightarrow 9s^2S_{1/2}$	0.28		$\rightarrow 7d^2D_{3/2}$	0.01
			$\rightarrow 7d^2D_{5/2}$	0.11	
			$\rightarrow 9s^2S_{1/2}$	0.23	
$10p^2P_{1/2}$	$\rightarrow 7s^2S_{1/2}$	0.04	$10p^2P_{3/2}$	$\rightarrow 7s^2S_{1/2}$	0.30
	$\rightarrow 6d^2D_{3/2}$	0.23		$\rightarrow 6d^2D_{3/2}$	0.01
	$\rightarrow 8s^2S_{1/2}$	0.09		$\rightarrow 6d^2D_{5/2}$	0.07
	$\rightarrow 7d^2D_{3/2}$	0.20		$\rightarrow 8s^2S_{1/2}$	0.18
	$\rightarrow 9s^2S_{1/2}$	0.11		$\rightarrow 7d^2D_{3/2}$	0.01
	$\rightarrow 8d^2D_{3/2}$	0.15		$\rightarrow 7d^2D_{5/2}$	0.07
	$\rightarrow 10s^2S_{1/2}$	0.18		$\rightarrow 9s^2S_{1/2}$	0.15
				$\rightarrow 8d^2D_{3/2}$	0.01
		$\rightarrow 8d^2D_{5/2}$	0.06		
			$\rightarrow 10s^2S_{1/2}$	0.16	

TABLE IV: Lifetimes of  $^{221}\text{Fr}$  levels.

Level	$\tau$ (ns)	Source
$10p^2P_{3/2}$	362(7)[3]	this work
$10p^2P_{1/2}$	553(21)[8]	this work
$10s^2S_{1/2}$	230.4(46)	[9]
$9p^2P_{3/2}$	179(5)[3]	this work
$9p^2P_{1/2}$	329(6)[2]	this work
$9s^2S_{1/2}$	107.53(90)	[10]
$8p^2P_{3/2}$	83.5(15)	[10]
$8p^2P_{1/2}$	149.3(35)	[10]
$8s^2S_{1/2}$	53.30(44)	[11]
$8d^2D_{5/2}$	95.9(19)	[9]
$8d^2D_{3/2}$	99.9(20)	[9]
$7p^2P_{3/2}$	21.02(11)	[12]
$7p^2P_{1/2}$	29.45(11)	[12]
$7d^2D_{5/2}$	67.7(29)	[13]
$7d^2D_{3/2}$	73.6(3)	[13]
$6d^2D_{5/2}$	1915(38)	[9]
$6d^2D_{3/2}$	559.2(11)	[9]
$7s^2S_{1/2}$	—	

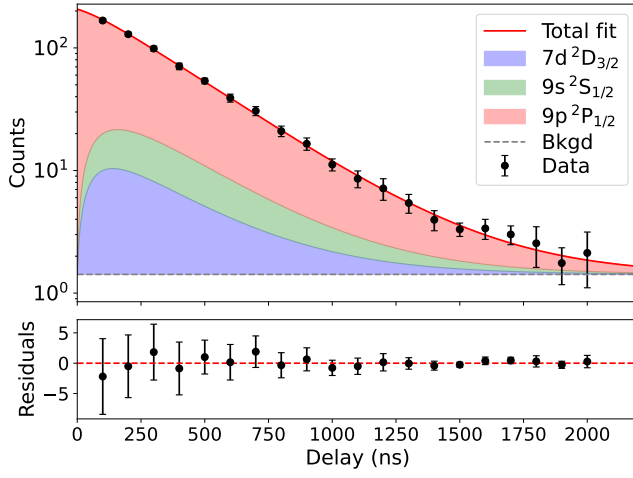


FIG. 3: Typical decay curves for the  $9p^2P_{1/2}$  level.

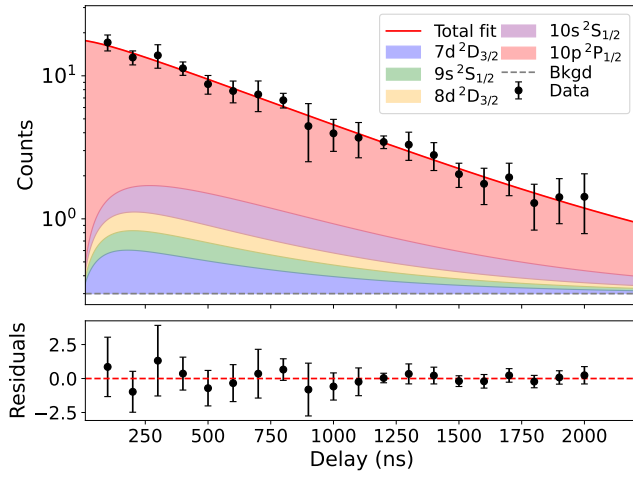


FIG. 4: Typical decay curves for the  $10p^2P_{1/2}$  level.

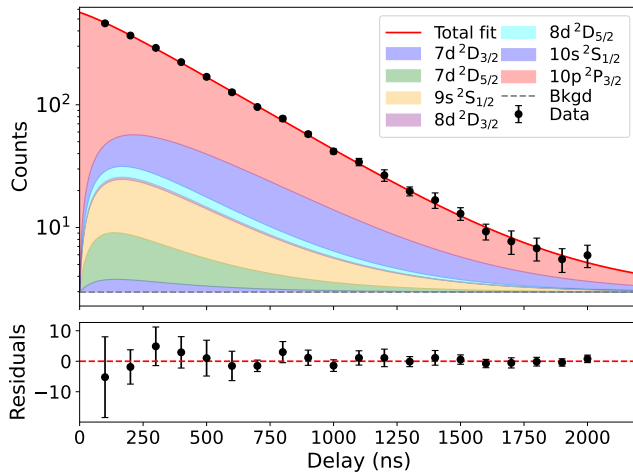


FIG. 5: Typical decay curves for the  $10p^2P_{3/2}$  level.

---

\* Corresponding author: pierre.lassegues@cern.ch

- [1] A. R. Vernon, J. Billowes, C. L. Binnersley, M. L. Bissell, T. E. Cocolios, G. J. Farooq-Smith, K. T. Flanagan, R. F. Garcia Ruiz, W. Gins, R. P. de Groote, *et al.*, *Spec. Acta B* **153**, 61 (2019).
- [2] R. P. de Groote, M. Verlinde, V. Sonnenschein, K. T. Flanagan, I. Moore, and G. Neyens, *Phys. Rev. A* **95**, 032502 (2017).
- [3] R. P. De Groote, I. Budinčević, J. Billowes, M. L. Bissell, T. E. Cocolios, G. J. Farooq-Smith, V. Fedosseev, K. Flanagan, S. Franchoo, R. G. Ruiz, and others, *Phys. Rev. Lett.* **115**, 132501 (2015).
- [4] D. C. Morton, *Astrophys. J. Suppl. Ser.* **130**, 403 (2000).
- [5] B. K. Sahoo and B. P. Das, *Phys. Rev. Lett.* **120**, 203001 (2018).
- [6] N. Yamanaka, B. K. Sahoo, N. Yoshinaga, T. Sato, K. Asahi, and B. P. Das, *EPJA* **53**, 54 (2017).
- [7] M. Athanasakis-Kaklamanakis, S. G. Wilkins, P. Lassègues, L. Lalanne, J. R. Reilly, O. Ahmad, M. Au, S. W. Bai, J. Berbalk, *et al.*, *Phys. Rev. A* **110**, L010802 (2024).
- [8] S. Aubin, E. Gomez, L. A. Orozco, and G. D. Sprouse, *Phys. Rev. A* **70**, 042504 (2004).
- [9] W. Van Wijngaarden and J. Xia, *J. Quant. Spec. Rad. Tr.* **61**, 557 (1999).
- [10] S. Aubin, E. Gomez, L. Orozco, and G. Sprouse, *Opt. Lett.* **28**, 2055 (2003).
- [11] E. Gomez, L. Orozco, A. P. Galvan, and G. Sprouse, *Phys. Rev. A* **71**, 062504 (2005).
- [12] J. Simsarian, L. A. Orozco, G. Sprouse, and W. Zhao, *Phys. Rev. A* **57**, 2448 (1998).
- [13] J. M. Grossman, R. P. Flliller, L. A. Orozco, M. R. Pearson, and G. D. Sprouse, *Phys. Rev. A* **62**, 062502 (2000).